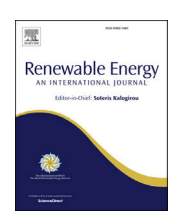


Contents lists available at ScienceDirect

Renewable Energy

journal homepage: www.elsevier.com/locate/renene



Thermal and structural evaluation of composite solar receiver tubes for Gen3 concentrated solar power systems



Shen Du a, b, Zexiao Wang a, Sheng Shen a, *

- ^a Department of Mechanical Engineering, Carnegie Mellon University, Pittsburgh, PA, USA, 15213
- b Key Laboratory of Thermo-Fluid Science and Engineering of Ministry of Education, School of Energy and Power Engineering, Xi'an Jiaotong University, Xi'an, Shaanxi, 710049, China

ARTICLE INFO

Article history: Received 30 December 2021 Received in revised form 21 February 2022 Accepted 25 February 2022 Available online 3 March 2022

Keywords:
Composite solar tube
Heat transfer
Structural analysis
Creep
Concentrated solar power

ABSTRACT

A composite solar receiver tube containing thermally conductive and high-temperature protective layers is proposed to improve its thermal and structural performances. Two combinations of materials, which are Inconel 718/nickel and 316 stainless steel/GRCop-84, are selected based on the similarity in their coefficients of thermal expansion. The solar-to-thermal energy conversion in conjunction with the fluid flow and heat transfer of supercritical carbon dioxide inside the solar tubes is analyzed by computational fluid dynamics. The thermal stress due to different solar tube designs is solved by finite element analysis based on the derived temperature field and pressure distribution. The results show that both maximum thermal stress and maximum temperature in solar tubes could be reduced by the composite design. The maximum thermal stress decreases by 4.1 MPa and 24.0 MPa respectively in Inconel 718/nickel and 316 stainless steel/GRCop-84 composite solar tubes. The performance improvement becomes more significant as the thickness of tube wall and intensity of solar radiation increase. Due to the surface temperature reduction, the entire thermal efficiency of solar tubes could increase by up to 1.3% and the creep issue of high-temperature protective materials can be alleviated.

© 2022 The Authors. Published by Elsevier Ltd. This is an open access article under the CC BY license (http://creativecommons.org/licenses/by/4.0/).

1. Introduction

Concentrated solar power (CSP) systems are moving towards the third generation (Gen3) with a key feature of elevated working temperature over 700 °C. The design goal is to achieve a high solarto-electric energy conversion efficiency while maintaining the safe operation of the system for 30 years [1,2]. Stringent requirements are therefore put forward for the material selection of solar tubes. in which both thermal and mechanical properties need to be concurrently taken into account. In the CSP system, the wall thickness of its receiver tube generally should be thin in order to minimize the temperature gradient and associated thermal stress. However, compared with existing CSP systems, the tube wall thickness of Gen3 systems could not be reduced further due to the corrosion and internal pressure of the heat transfer fluid, especially when supercritical carbon dioxide (sCO₂) is applied. Particularly, the stainless steel currently used in existing CSP systems and the nickel-based superalloy as the potential candidate for Gen3

systems usually suffer from low thermal conductivity, which leads to prohibitively high temperature and high stress on the solar receiver tube.

Due to the measurement challenges of solar receiver tubes at high temperatures, theoretical approaches or numerical methods are commonly used to investigate the stress induced by temperature gradient and pressure. Conroy et al. [3] reviewed the thermal and mechanical modelling on tubular solar receivers for the solar tower systems. The recent progresses for the thermal modelling in the tube-level and receiver-level were presented. The numerical methods for the thermal and pressure induced stress calculations and the mechanical reliability estimation were shown. Theoretically, thermoelastic stress equations [3] can be used by assuming that the temperature gradient in the radial direction of the solar tube is the most critical component. Neises et al. [4] evaluated a solar receiver tube under 25 MPa sCO₂ operating pressure. The pressure induced stress was calculated based on the thick-walled tube model and the thermal stress was determined by considering only the radial temperature difference. It was found that the largest tangential and longitudinal total stresses locate at the inner surface of the tube. Nithyanandam and Pitchumani [5] investigated

E-mail address: sshen1@cmu.edu (S. Shen).

^{*} Corresponding author.

the thermal and mechanical performances of an sCO₂ solar tube receiver with high internal pressure and high outlet temperature, and the requirement of lifetime over 10000 cycles and 100000 h was also evaluated. Based on the heat transfer analysis and theoretical stress calculation, the influence of the tube radius, tube length, mass flow rate, and tube wall thickness on the creep and fatigue failures were determined. Ortega et al. [6] conducted static thermal-structural analysis by importing the non-uniform temperature distribution on the solar tube as the boundary condition in the finite element analysis. The stress and strain distributions of the tube were calculated while fatigue and creep damages were evaluated based on the cumulative damage approach. Montoya et al. [7] specifically considered the influence of mechanical boundary conditions on the solar tube stress. The solar panel in the Gemasolar solar plant was selected to study the effect of clips which limits the deflection of the tube. The clips in the solar panel could prevent the solar tube from the evident bending, but they introduced extra equivalent stress which tripled its original value without clips. Logie et al. [8] investigated thermal stress in a solar receiver tube using molten salt or liquid sodium as the heat transfer fluid, respectively. Compared with molten salt, the liquid sodium was preferred because its higher thermal conductivity leads to the reduction of overall tube temperature and thermal stress. The influence of thermal conductivity of tube materials was also analyzed and the higher thermal conductivity tended to decrease the peak thermal stress. Wang et al. [9] developed a thermal-fluidmechanical numerical model for the sCO₂ tubular receiver panel under non-uniform solar flux distribution. The flow arrangement was designed to match the solar flux distribution, which is beneficial of reducing the thermal radiative loss and the thermal stress level. A matching factor between the solar flux distribution and the flow allocation was therefore proposed for indicating the receiver thermo-mechanical performances. Thermal and mechanical performance evaluations were also conducted by Wang et al. [10,11] for the solar tube in the parabolic trough system considering the nonuniform solar flux distribution and buoyancy effects. Chen et al. [12] investigated the fatigue-creep damage of the SCO₂ solar tube in the solar tower system by applying the conjugate heat transfer and the theoretical stress models. Based on the linear damage accumulation theory, the influences of sCO₂ flow rate, tube wall thickness, and the tube radius on the thermal performance and fatiguecreep damage of the solar tube were studied. Thermal performance and thermal stress analyses were also done by Chen et al. [13] for the cavity receiver in the parabolic dish collector. The up-flow and down-flow schemes for the cavity receiver were considered and geometrical parameters as well as operating parameters were also investigated.

Furthermore, many studies were focused on the improvement of mechanical performance of solar receivers. Other than regular concentric cylinder solar receivers, an eccentric tube was proposed for alleviating thermal stress [14]. The influences of eccentricity and oriented angle on the thermal stress distribution of the eccentric solar receiver were investigated. Optimized eccentricity and oriented angle of 90° were recommended according to the parametric studies. Moreover, since the radial temperature gradient is the key factor to determine the thermal stress in solar receivers, many efforts have been made to reduce the radial temperature difference by introducing thermally conductive materials. Thermal stress analyses of solar receiver tubes using different materials were conducted by Wang et al. [15]. The temperature and thermal stress distributions were compared for the solar receiver tubes made from stainless steel, aluminum, copper, and silicon carbide, respectively. It was found that the temperature gradient and effective stress could be significantly reduced by introducing materials with high thermal conductivity. However, the corrosion, high-temperature creep and fatigue of the materials were not considered. Flores and Almanza [16] experimentally tested the stress induced deflection of the copper-steel bimetallic absorber. A mechanically bonded copper-steel bimetallic tube was prepared through high pressure. Compared with the steel based absorber, the deflection in the bimetallic absorber was decreased to 10 mm from over 50 mm due to the decrease of thermal stress. This double-layer structure was also adopted in the study by Khanna et al. [17]. The heat transfer performance and the mitigation of thermal stress by bimetallic solar tube receivers were analytically investigated. The results showed that the structure with the high thermal conductivity material in the outer layer could effectively minimize the circumferential temperature non-uniformity while dramatically reducing the thermal stress. Moreover, Montoya et al. [18] investigated the influence of longitudinal clips on the thermal stress and deflection of the solar tube based on the analytical methodology. The distance of longitudinal supports and the aiming strategy could be optimized for reducing the maximum equivalent elastic stress and deflection of the solar tube.

However, existing multiplayer solar tube designs have mainly focused on double-layer structures, in which the protection of the thermally conductive material layer has not been considered for both oxygen in atmosphere and heat transfer fluid. Furthermore, most of the related studies applied simple theoretical stress models to calculate the thermal and pressure induced stresses. In this work, a new triple-layer composite solar tube consisting of two hightemperature protective layers on the two sides and a thermally conductive layer in the middle is demonstrated. The wholistic numerical models incorporating fluid flow, heat transfer, structural analysis with temperature-dependent thermochemical and thermophysical properties are developed. Hence, the solar energy conversion and stress issue of the triple-layer composite solar tube can be fully analyzed by computational fluid dynamics and finite element method. From the numerical simulations, the influences of material selection, tube wall thickness, and solar radiation intensity on the thermal and structural performances of the triple-layer composite solar tubes are thoroughly studied. Finally, the potential manufacturing methods of the triple-layer composite solar tubes for real CSP applications are discussed.

2. Numerical model

2.1. Physical model of composite solar tubes

A composite solar receiver tube consisting of two protective layers and an intermediate thermally conductive layer is designed in Fig. 1. Two combinations of materials are selected in the study. One combination uses Inconel 718 as the protective layer and pure nickel as the thermally conductive layer, while the other selects 316 stainless steel and copper alloy GRCop-84 as the protective and the thermally conductive materials, respectively. The total length L of the tube is set to be 0.5 m, which is sufficient to reveal the stress distribution inside the solar tube. Two sets of inner diameter d_{in} (6 mm and 7 mm) and wall thickness t (3 mm and 4 mm) are selected to investigate the influence of wall thickness on heat transfer and mechanical performances. The non-uniform solar flux is irradiated on the surface of the tube, and an idealized distribution shown by Equation (1) is used [19]. The Gaussian distribution is adopted along the tube axial direction, while a sinusoidal distribution is applied in the circumferential direction. In Equation (1), q_{max} is the maximum solar flux, φ represents the angle with respect to y-z plane, and μ and σ depict the expectation and the standard deviation of the Gaussian distribution, respectively. The highpressure sCO₂ is used as the heat transfer fluid and the flow direction is along the z-axis.

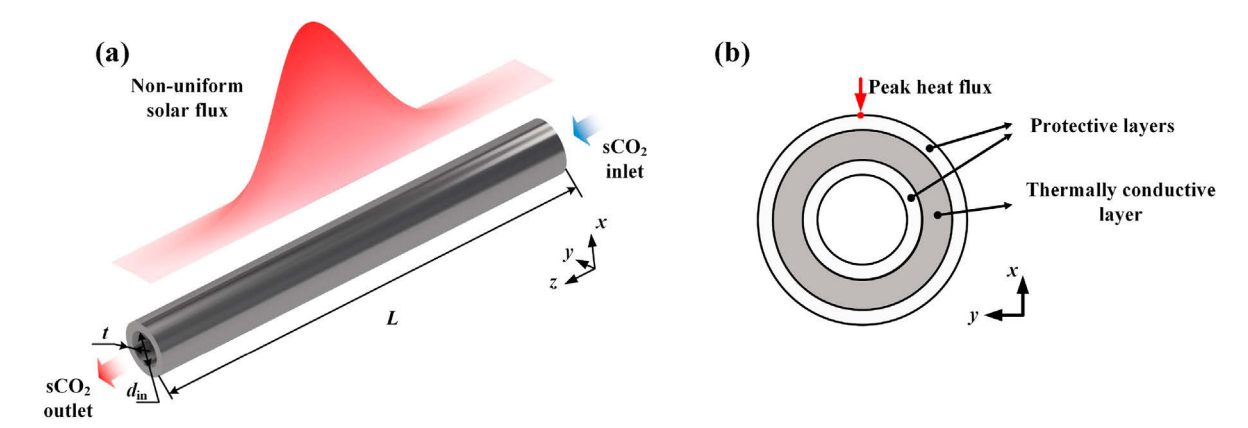


Fig. 1. Illustration of composite solar tubes. (a) Solar tube under a non-uniform solar flux, and (b) Cross-section of the composite tube.

$$q(z,\varphi) = q_{\text{max}} \cdot \cos \varphi \cdot \exp\left\{-\frac{1}{2} \left(\frac{z-\mu}{\sigma}\right)^2\right\}$$
 (1)

2.2. Fluid flow and heat transfer models of sCO₂ in the solar tube

The fluid flow and heat transfer of sCO₂ in the solar tube are depicted by the Reynolds-averaged governing equations, which are presented by Equations (2)–(4). Moreover, the heat conduction in the solar tube is shown by Equation (5). In these equations, u, p, $T_{\rm f}$ and $T_{\rm s}$ represent velocity, pressure, fluid temperature, and solid temperature respectively. ρ , μ , c_p and $\lambda_{\rm f}$ stand for density, dynamic viscosity, specific heat and thermal conductivity of sCO₂, respectively. $\lambda_{\rm s}$ represents the thermal conductivity of solid materials. $-\rho \overline{u_i'u_j'}$ and $-\rho \overline{u_j'T_f'}$ are introduced as additional terms due to the effect of turbulence, which are calculated based on the standard k- ε model

$$\frac{\partial}{\partial x_i}(\rho u_j) = 0 \tag{2}$$

$$\frac{\partial}{\partial x_{i}}(\rho u_{i}u_{j}) = -\frac{\partial p}{\partial x_{i}} + \frac{\partial}{\partial x_{j}} \left(\mu \frac{\partial u_{i}}{\partial x_{j}} - \rho \overline{u'_{i}u'_{j}}\right) (i = 1, 2, 3) \tag{3}$$

$$\frac{\partial}{\partial x_{j}} \left(\rho u_{j} T_{f} \right) = \frac{\partial}{\partial x_{j}} \left[\frac{\lambda_{f}}{c_{p}} \frac{\partial T_{f}}{\partial x_{j}} - \rho \overline{u'_{j} T'_{f}} \right]$$
(4)

$$\frac{\partial}{\partial x_j} \left(\lambda_s \frac{\partial T_s}{\partial x_j} \right) = 0 \tag{5}$$

The turbulence kinetic energy k and its rate of dissipation ε are derived from transport Equations (6) and (7). The turbulent viscosity $\mu_{\rm t}$ is computed with k and ε ($\mu_{\rm t} = c_\mu \rho k^2 / \varepsilon$) where c_μ is a constant. G_k and G_b are the generation of turbulence kinetic energy due to the mean velocity gradients and buoyancy, respectively. $C_{1_{\mathcal{B}}}$ $C_{1_{\mathcal{B}}}$ G_k , and G_{ε} are constants that retain the default value in the standard k- ε model [20].

$$\frac{\partial}{\partial x_j} (\rho k u_j) = \frac{\partial}{\partial x_j} \left[\left(\mu + \frac{\mu_t}{\sigma_k} \right) \frac{\partial k}{\partial x_j} \right] + G_k + G_b - \rho \varepsilon$$
 (6)

(1)
$$\frac{\partial}{\partial x_{j}} \left(\rho \varepsilon u_{j} \right) = \frac{\partial}{\partial x_{j}} \left[\left(\mu + \frac{\mu_{t}}{\sigma_{\varepsilon}} \right) \frac{\partial \varepsilon}{\partial x_{j}} \right] + C_{1\varepsilon} \frac{\varepsilon}{k} \left(G_{k} + C_{3\varepsilon} G_{b} \right) - C_{2\varepsilon} \rho \frac{\varepsilon^{2}}{k}$$
(7)

At the inlet of the solar tube, the sCO₂ with constant mass flow rate of 0.08 kg/m² and constant inlet temperature of 773.15 K is used. The nominal application conditions for sCO2 are summarized in Ref. [21] and the working pressure is in the range between 15 and 35 MPa. The absolute pressure of sCO₂ is 20 MPa, which fits the Brayton cycle known as the best-fit power cycle for increasing CSP system thermo-electric conversion efficiency. At the outlet, the pressure outlet boundary is used. The inner wall of the solar tube is considered as a non-slip and coupled wall while the outer surface of the solar tube is irradiated by solar flux. Energy losses on the outer surface occur through both emission and convection. The incident solar flux is shown by Equation (1) and its peak flux is set to be 700 kW/ m^2 . The selective coating with a solar absorptivity of 0.9 and an infrared emissivity of 0.4 is coated on the solar tube. The convective loss is considered by assuming a constant convective heat transfer coefficient of 15 W/($m^2 \cdot K$).

2.3. Static structural model

The stress in the solar tube due to temperature gradient and inner pressure of sCO₂ is analyzed by finite element analysis (FEA) model in ANSYS Workbench. The static structural module is used and the computational fluid dynamics (CFD) results such as the temperature and pressure distributions on the solar tube are imported as loads. The displacement of the solar tube in the circumferential direction is fixed and it is assumed to be freely expanded in the axial direction due to the designed strain relief structures in solar tubes.

2.4. Material selection and material properties

sCO₂ is selected as the heat transfer fluid in solar tubes because of its potential to achieve high cycle efficiency and attractive advantages such as low critical temperature and high thermodynamic efficiency. The density, specific heat, thermal conductivity, and viscosity of the sCO₂ are taken from the NIST (National Institute of Standards and Technology) real gas models in ANSYS Fluent. This model provides precise thermophysical properties of sCO₂ in wide pressure and temperature ranges.

As for the solar tube material, two combinations of solid materials are selected based on the similarity of coefficients of thermal expansion and the applicability at high temperature. The first

combination is Inconel 718 and pure nickel. Nickel-based superalloys offer excellent mechanical properties and high corrosion resistance at high temperatures and therefore are considered as promising materials for Gen3 CSP systems. Pure nickel has relatively poor mechanical properties compared with Inconel 718 but the thermal conductivity is higher. The other combination is 316 stainless steel together with copper alloy GRCop-84. 316 stainless steel is widely used as one solar tube material in current CSP systems, while GRCop-84 is a thermally conductive copper alloy with good mechanical properties at high temperatures. The temperature-dependent thermophysical and mechanical properties of Inconel 718, nickel, 316 stainless steel, and GRCop-84 are applied in this study. The correlations of thermal conductivity (λ_s) of materials are derived from data in literature, as summarized in Table 1.

Moreover, coefficients of thermal expansion (α) and Young's modulus (E) are used in the static structural model. The data in references are directly stored in engineering database in ANSYS workbench for the mechanical properties of Inconel 718 [22], nickel [26,27], and 316 stainless steel [28,29]. As for GRCop-84, the coefficient of thermal expansion and Young's modulus are estimated from experimental results in Ref. [30].

3. Model validation

3.1. Heat transfer model validation

The numerical model for the heat transfer of sCO₂ inside a cylindrical tube is validated based on the experiment results in Ref. [31]. According to the experiment setup, the inner diameter of the tube is 6 mm and an average heat flux of 12 kW/m² is placed outside the tube to cool down sCO₂. The inlet temperature is assumed to be constant and uniform. The mass flow rate and inlet

Table 1Thermal conductivity of solar tube materials.

Material	Thermal conductivity $(W/(m \cdot K))$
Inconel 718 [22]	0.0156 T + 6.29
Nickel [23]	0.0212 T + 50.58
316 stainless steel [24]	0.0157 T + 9.28
GRCop-84 [25]	$-1.33 \times 10^{-4} \cdot T_s^2 + 0.179 \cdot T_s + 243.8$

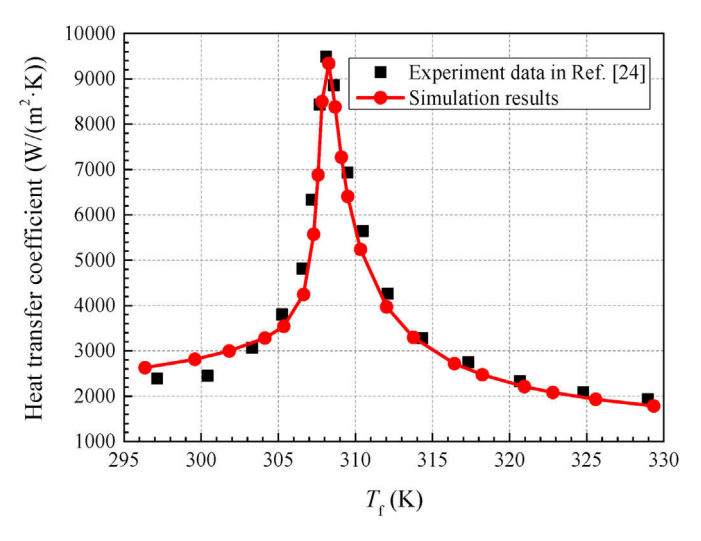


Fig. 2. Comparison of heat transfer coefficients in the simulation with experiment data.

pressure are fixed to $400 \text{ kg/(m}^2 \cdot \text{s)}$ and 8 MPa, respectively. The comparison of simulation results with experiment data in Ref. [31] is presented in Fig. 2. It is seen that the variation trend of convective heat transfer coefficients with the average fluid temperature is well captured by the numerical model. The simulation results agree well with experiment data, which indicates the accuracy of the heat transfer model.

3.2. Static structural model validation

The temperature distribution and pressure load influence the FEA results, and a theoretical model is used to validate the static structural model. In a cylindrical tube with radial temperature gradient and uniform inner pressure, the thermal and pressure stress components in the radial, tangential, and axial directions could be described by Equations (8) - (13) [4]. Considering that the displacement of the tube is free along the axial direction, the axial component of pressure stress is assumed to be zero in the theoretical calculation.

$$\sigma_{\text{thermal},r} = \frac{\alpha E \Delta T}{2(1-\nu) \ln\left(\frac{r_0}{r_i}\right)} \left[-\ln\frac{r_0}{r} - \frac{r_i^2}{r_0^2 - r_i^2} \left(1 - \frac{r_0^2}{r^2}\right) \ln\left(\frac{r_0}{r_i}\right) \right]$$
(8)

$$\sigma_{\text{thermal},\theta} = \frac{\alpha E \Delta T}{2(1-\nu)\ln\left(\frac{r_0}{r_i}\right)} \left[1 - \ln\frac{r_0}{r} - \frac{r_i^2}{r_0^2 - r_i^2} \left(1 + \frac{r_0^2}{r^2}\right) \ln\left(\frac{r_0}{r_i}\right) \right]$$
(9)

$$\sigma_{\text{thermal,a}} = \frac{\alpha E \Delta T}{2(1-\nu) \ln\left(\frac{r_o}{r_i}\right)} \left[1 - 2 \ln\frac{r_o}{r} - \frac{2r_i^2}{r_o^2 - r_i^2} \ln\left(\frac{r_o}{r_i}\right) \right]$$
(10)

$$\sigma_{\text{pressure},r} = \frac{p_i r_i^2}{r_0^2 - r_i^2} \left(1 - \frac{r_0^2}{r^2} \right)$$
 (11)

$$\sigma_{\text{pressure},\theta} = \frac{p_{i}r_{i}^{2}}{r_{0}^{2} - r_{i}^{2}} \left(1 + \frac{r_{0}^{2}}{r^{2}}\right)$$
 (12)

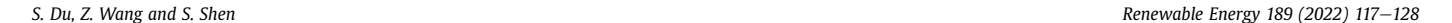
$$\sigma_{\text{pressure,a}} = \frac{p_i r_i^2}{r_0^2 - r_i^2} \tag{13}$$

A simulation case is selected based on the study by Ortega et al. [6]. The outer diameter and wall thickness of the tube are 12.7 mm and 2.1082 mm, respectively. The radial temperature difference is 20 K and a pressure of 20 MPa is loaded on the inner wall of the tube. The equivalent thermal stress, pressure stress, and total stress calculated by FEA and theoretical equations are shown in Fig. 3. It is noticed that the results from FEA and theoretical equations agree well with each other, and FEA could be further applied to investigate the solar tube with complex temperature and pressure distributions.

4. Results and discussion

4.1. Verification of the design concept

As mentioned previously, two combinations of protective and thermally conductive materials are selected based on the similarity in coefficients of thermal expansion. The solar tubes with an inner diameter of 6 mm and a wall thickness of 3 mm are firstly analyzed



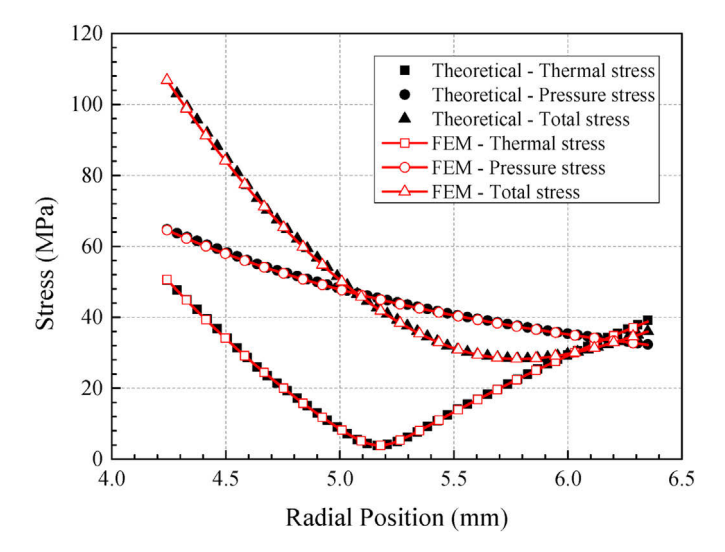


Fig. 3. Comparison of FEA stress results with those from theoretical models.

to prove the feasibility of our composite tube design. The tube wall is divided identically into three layers with each layer's thickness of 1 mm. The material assignment in each layer of the solar tubes is summarized in Table 2.

4.1.1. Inconel 718/Nickel design

The temperature distributions in different sections (100/175/250/325/400 mm) of Tube A and Tube B are presented in Fig. 4. Since the solar energy is irradiated from the positive X direction in the Gaussian distribution, a relatively higher temperature is found at the center of the solar tube in the positive X direction. Compared with the solar tube made entirely from Inconel 718, the maximum temperature of the composite tube decreases by 40.7 K and the temperature field becomes more uniform by adding the thermally conductive layer of nickel.

Based on the temperature distributions, the equivalent thermal stress is determined by FEA for each tube as shown in Fig. 5. For the solar tube with Inconel 718 only, the overall thermal stress increases as the temperature gradient increases, and the maximum thermal stress is located at the inner wall in the center part of the tube. When nickel is added in the middle layer, it is found that the thermal stress in the middle layer increases, but the maximum thermal stress is alleviated. The maximum thermal stress is still found at the inner wall in the center section of the tube, but it decreases from 110.1 MPa to 102.1 MPa.

The high pressure of sCO_2 also induces stress in the solar tube. The equivalent total stress considering the effects of temperature gradient and internal sCO_2 pressure is shown in Fig. 6. The maximum total stress is larger than the maximum thermal stress because the two maximum stresses are both tensile stress and do not compensate with each other. However, when considering the pressure induced stress, the alleviation of total stress by inserting the nickel in the middle layer of the solar tube is not significant, as the maximum total stress only decreases by 4.1 MPa.

4.1.2. 316 stainless steel/GRCop-84 design

The selection of GRCop-84 with extremely high thermal conductivity is to reveal the potential improvement of thermal stress by the composite solar tube design. The temperature distributions in different sections (100/175/250/325/400 mm) of Tube C and Tube D are presented in Fig. 7. It is noticed that the high temperature region in solar tube is removed in the composite solar tube. GRCop-84 offers a ten times higher thermal conductivity than 316 stainless steel and the heat conduction in the entire tube is more efficient. The maximum temperature decreases from 970 K to 901 K and temperature differences in the radial, circumferential and axial directions are well flattened.

The equivalent thermal stress and total stress of the solar tube with 316 stainless steel only and the composite solar tube with GRCop-84 in the middle layer are shown in Fig. 8 and Fig. 9, respectively. Compared with Tube A, the thermal stress and total stress distributions in Tube C are nearly identical because of the similarity of temperature distribution in solar tubes with single materials. However, the stress distributions in the 316 stainless steel/GRCop-84 composite tube (Tube D) are completely changed. The stress in the middle of the solar tube is relatively small due to the mild temperature gradient and relatively soft mechanical properties of GRCop-84. The maximum thermal stress and total stress are significantly decreased by 24.0 MPa and 30.7 MPa respectively using the composite solar tube design. It is seen from Section 2.4 that the mismatch of mechanical properties (coefficient of thermal expansion and Young's modulus) between 316 stainless steel and GRCop-84 are larger as compared with Tube B. However. the higher thermal conductivity of GRCop-84 could balance the extra stress induced by the property mismatch and dramatically decrease the overall temperature and stress of the solar tube.

4.2. Influence of wall thickness

Due to the larger internal pressure caused by sCO₂ and the corrosion issue, it is helpful to increase the wall thickness for the long-term operation of solar receivers. However, it is known that the thermal stress depends on the wall thickness of solar tubes. A larger wall thickness induces a larger temperature gradient and severer thermal stress. In this case, the solar tubes with the inner diameter of 7 mm and the wall thickness of 4 mm are investigated to reveal the performance of the composite tube design with a thicker wall thickness. The tube wall is also divided into three layers with the protective layer thickness and thermally conductive layer thickness set to be 1 mm and 2 mm, respectively. Table 3 shows four solar tube studied in this work.

As illustrated in literature [3], the thermal stress in solar tubes mainly depends on the radial temperature gradient in some cases. Fig. 10 shows the temperature difference between the outer and the inner walls as a function of angular position in the center section of solar tubes. The zero angular position is defined in the area with the largest solar flux.

It is observed that the composite tube design could efficiently decrease the radial temperature gradient. Such an improvement becomes more evident as the wall thickness of the solar tube gets larger. For the Inconel 718/Nickel design, the largest radial

Table 2 Material assignment in composite solar tubes (t = 3 mm).

Tube number	Dimension	Inner layer	Middle layer	Outer layer
A	$d_{\text{in}} = 6 \text{ mm t} = 3 \text{ mm}$	Inconel 718	Inconel 718	Inconel 718
В		Inconel 718	Nickel	Inconel 718
C		316 stainless steel	316 stainless steel	316 stainless steel
D		316 stainless steel	GRCop-84	316 stainless steel

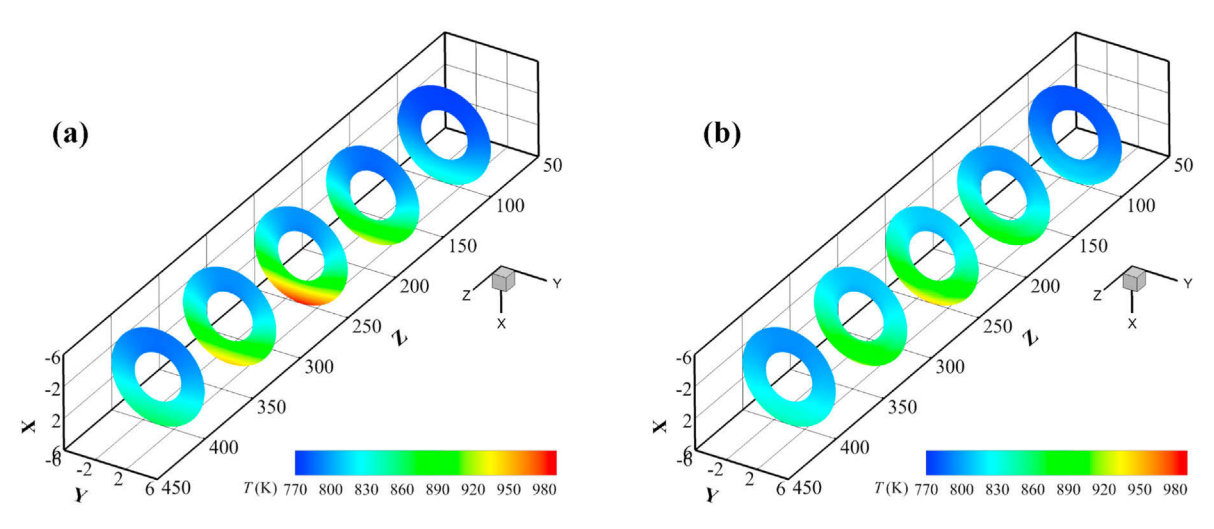


Fig. 4. Temperature distribution of solar tubes ($d_{in} = 6$ mm, t = 3 mm). (a) Conventional solar tube with Inconel 718 only, and (b) Composite solar tube with Inconel 718/Nickel.

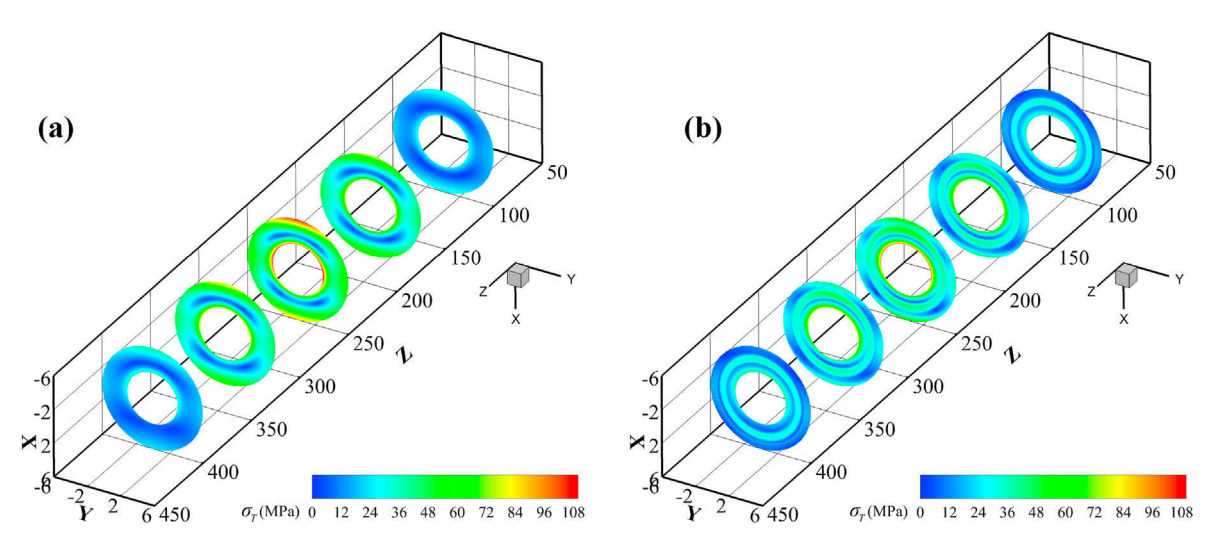


Fig. 5. Thermal stress distribution of solar tubes ($d_{\rm in}=6$ mm, t=3 mm). (a) Conventional solar tube with Inconel 718 only, and (b) Composite solar tube with Inconel 718/Nickel.

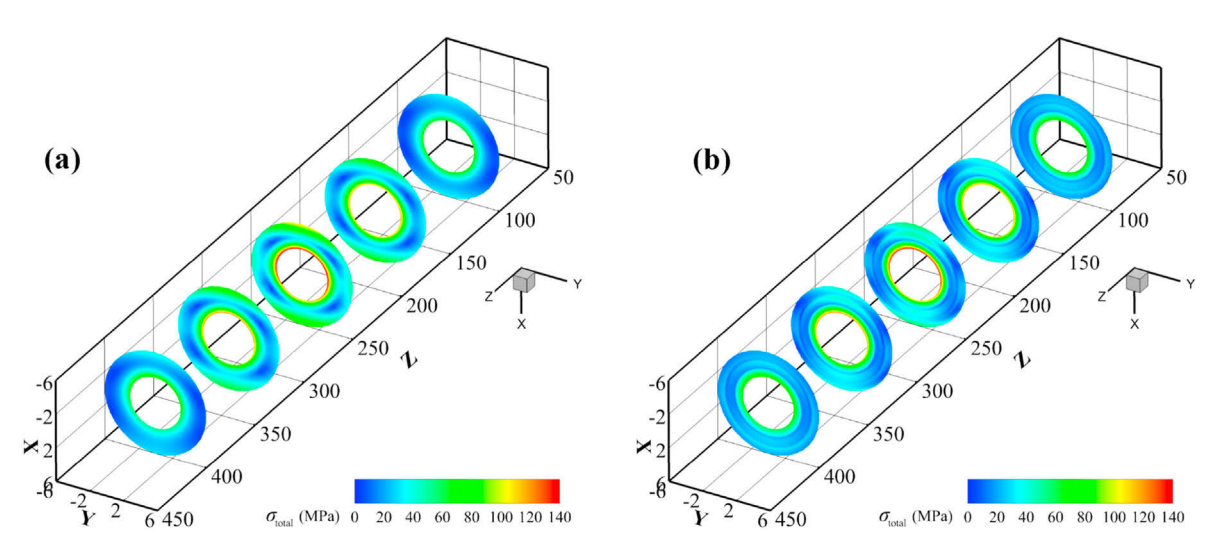


Fig. 6. Total stress distribution of solar tubes ($d_{in} = 6 \text{ mm}$, t = 3 mm). (a) Conventional solar tube with Inconel 718 only, and (b) Composite solar tube with Inconel 718/Nickel.

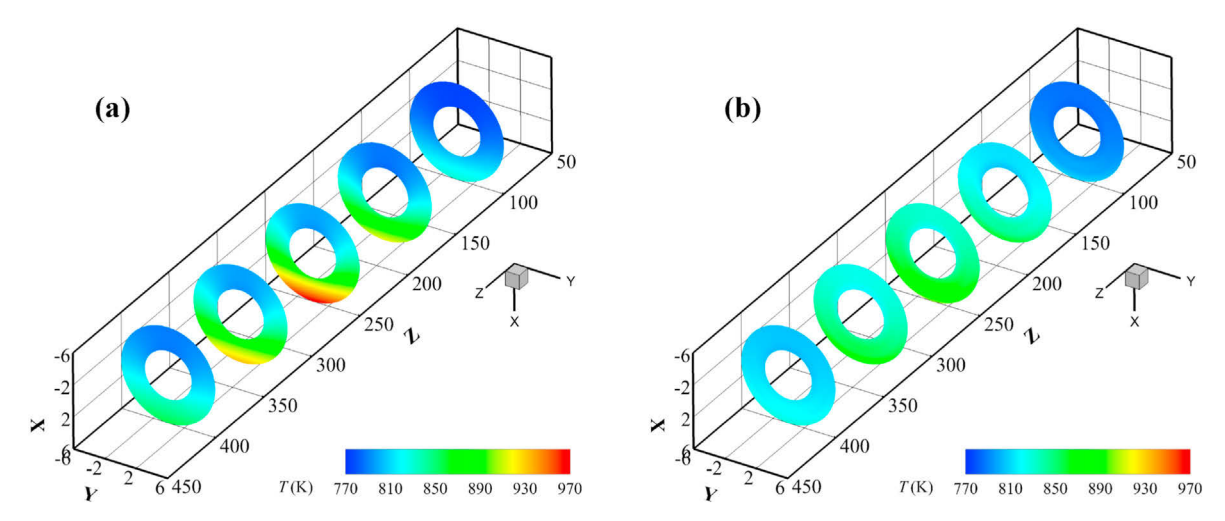


Fig. 7. Temperature distribution of solar tubes ($d_{\text{in}} = 6 \text{ mm}$, t = 3 mm). (a) Conventional solar tube with 316 stainless steel only, and (b) Composite solar tube with 316 stainless steel/GRCop-84.

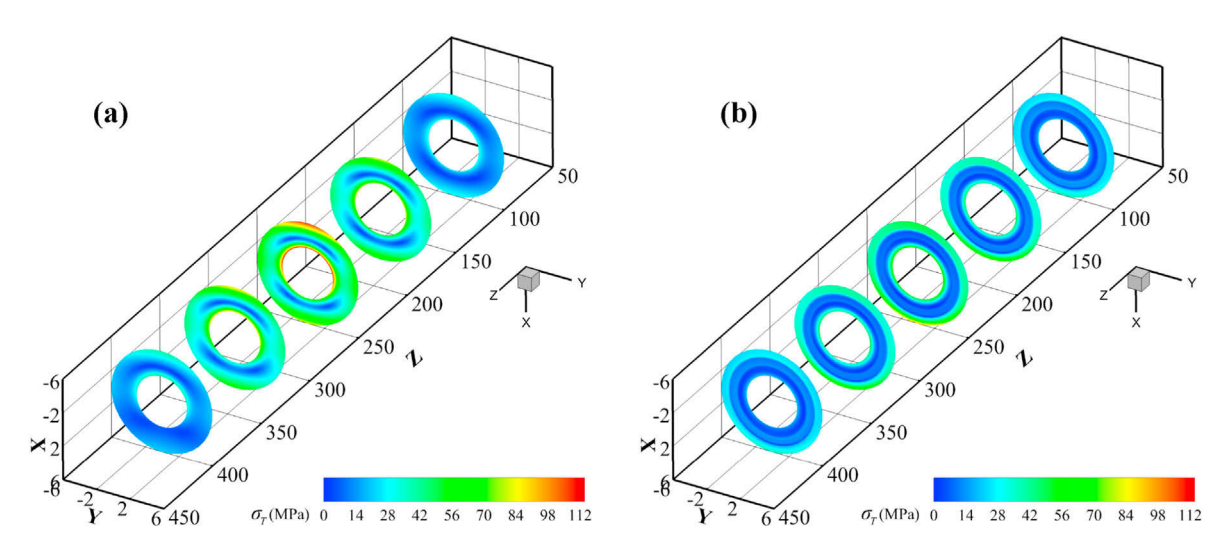


Fig. 8. Thermal stress distribution of solar tubes ($d_{\rm in}=6$ mm, t=3 mm). (a) Conventional solar tube with 316 stainless steel only, and (b) Composite solar tube with 316 stainless steel/GRCop-84.

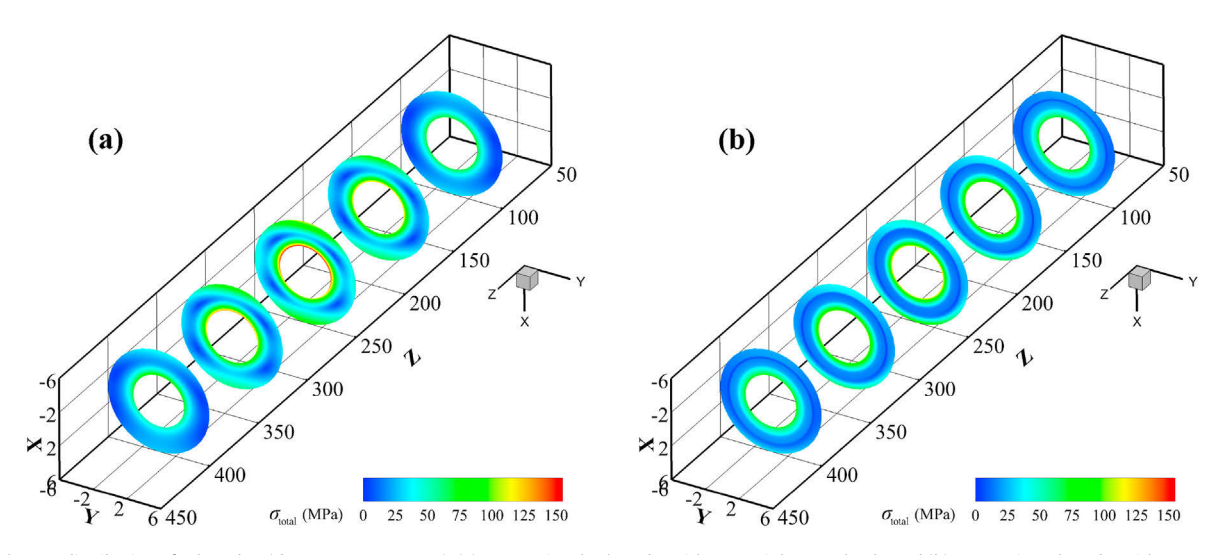


Fig. 9. Total stress distribution of solar tubes ($d_{in} = 6 \text{ mm}$, t = 3 mm). (a) Conventional solar tube with 316 stainless steel only, and (b) Composite solar tube with 316 stainless steel/GRCop-84.

Table 3 Material assignment in composite solar tubes (t = 4 mm).

Number	Dimension	Inner layer	Middle layer	Outer layer
E	$d_{in} = 7 \text{ mm t} = 4 \text{ mm}$	Inconel 718	Inconel 718	Inconel 718
F		Inconel 718	Nickel	Inconel 718
G		316 stainless steel	316 stainless steel	316 stainless steel
Н		316 stainless steel	GRCop-84	316 stainless steel

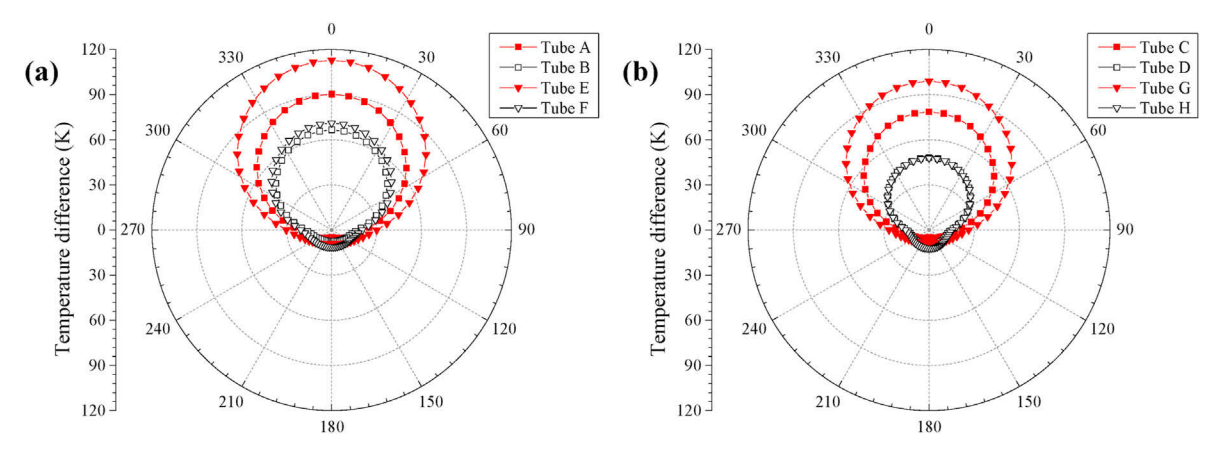


Fig. 10. Temperature difference of the outer and the inner walls of solar tubes. (a) Inconel 718/Nickel design, and (b) 316 stainless steel/GRCop-84 design.

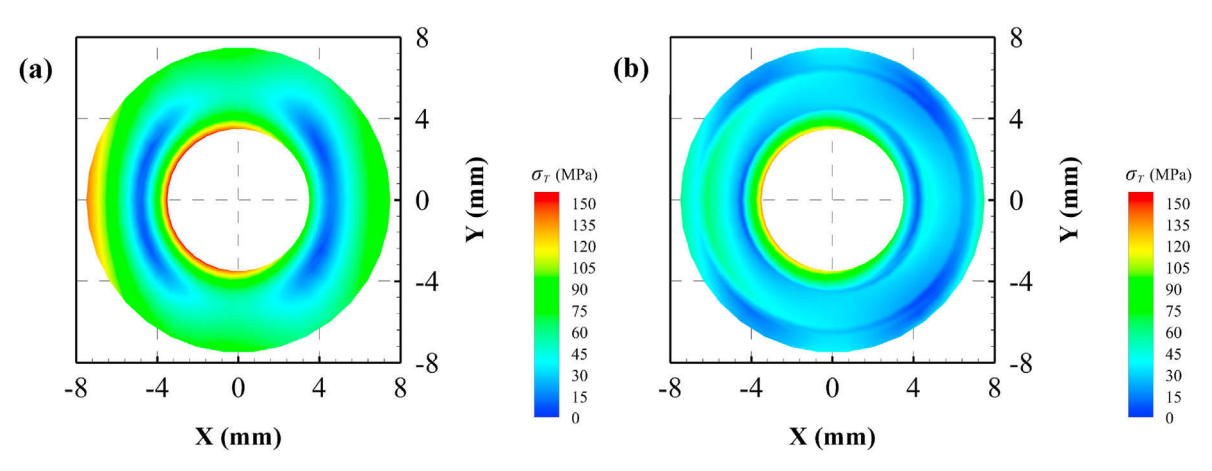


Fig. 11. Thermal stress distribution of solar tubes ($d_{\rm in}=7$ mm, t=4). (a) Conventional solar tube with Inconel 718 only, and (b) Composite solar tube with Inconel 718/Nickel.

temperature difference decreases by 23.7 K and 41.8 K respectively when the tube wall thicknesses are 3 mm and 4 mm. Meanwhile, due to the extremely high thermal conductivity of GRCop-84, the radial temperature difference is almost unchanged for the composite solar tube in the 316 stainless steel/GRCop-84 design when the total thickness of the solar tube increases by 1 mm.

Based on the aforementioned analyses, the maximum thermal stress and total stress are found at the center part of the solar tube, which is considered as the most fragile location. Therefore, the thermal stress distribution in the center section of Tube E and Tube F is shown in Fig. 11, while those of Tube G and Tube H are plotted in Fig. 12. Firstly, the overall thermal stress distribution is similar to that in the solar tube with the wall thickness of 3 mm. But the larger wall thickness increases the thermal stress level in all the solar tubes due to the larger temperature gradient. Secondly, the improvement of thermal stress for the composite tube design becomes more evident in both the Inconel 718/Nickel and 316 stainless steel/GRCop-84 designs. Compared with the solar tube made

from Inconel 718 only, the composite solar tube with nickel in the middle layer could decrease the maximum thermal stress from 154.7 MPa to 135.9 MPa. Moreover, by inserting GRCop-84 in the middle layer, the maximum thermal stress drops from 167.6 MPa to 99.7 MPa.

For a clear comparison between composite solar tubes in different material combinations and conventional solar tubes, the maximum solar tube temperature, maximum thermal stress, and maximum total stress for Tube A to Tube H are summarized in Table 4. Considering that the thermally conductive layer decreases the solar tube surface temperature, the thermal efficiency could be potentially improved due to the limited thermal emission loss. From Table 4, it could be concluded that the maximum thermal stress decreases significantly as the tube wall thickness and thermal conductivity of the material in the middle layer increase. The largest absolute and relative decreases in maximum thermal stress are 77.7 MPa and 37.3% for the 316 stainless steel/GRCop-84 design with the 4 mm tube wall thickness. On the other hand, a slight



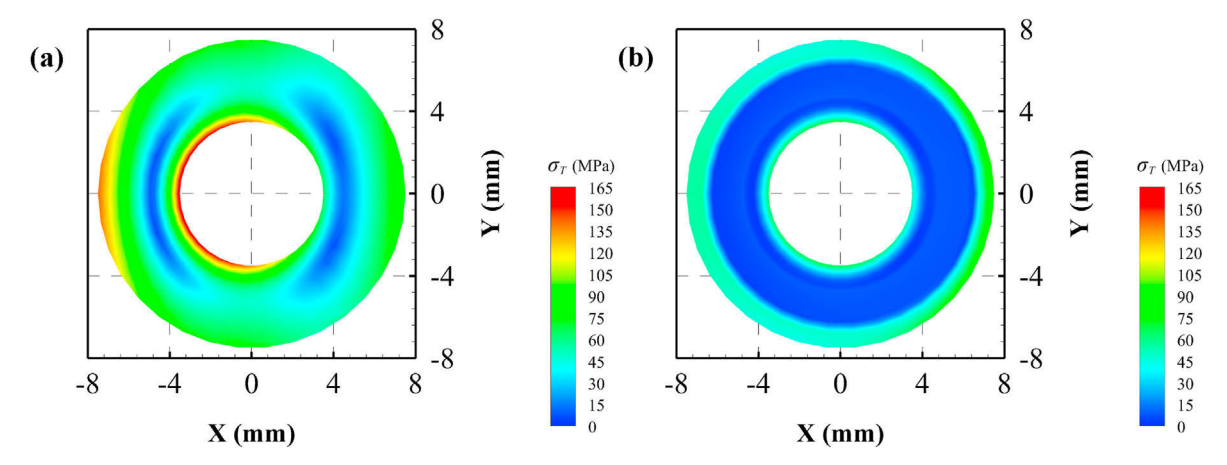


Fig. 12. Thermal stress distribution of solar tubes ($d_{in} = 7 \text{ mm}$, t = 4 mm). (a) Conventional solar tube with 316 stainless steel only, and (b) Composite solar tube with 316 stainless steel/GRCop-84.

Table 4 Performance of the solar tubes.

Tube	Dimension	T _{max} (K)	η _t (%)	$\sigma_{t,max}$ (MPa)	σ _{total,max} (MPa)
Α	$d_{\rm in} = 6 \text{ mm t} = 3 \text{ mm}$	985.4	75.6	110.1	146.6
В		944.7	76.0	102.1	142.6
C		970.0	75.8	113.9	155.0
D		901.0	76.2	89.9	124.3
E	$d_{in} = 7 \text{ mm t} = 4 \text{ mm}$	1057.0	74.1	154.7	195.4
F		986.8	74.8	135.9	176.2
G		1038.1	74.4	167.6	208.1
Н		932.7	75.1	99.7	130.4

increase in thermal efficiency could be seen for the composite solar tube, which are 0.4% and 0.7% for the composite solar tubes with 3 mm and 4 mm wall thicknesses, respectively. The thermal emission loss takes place in the entire outer surface of solar tubes and mainly determined by the surface temperature. Even though the maximum solar tube temperature is dramatically decreased. the average temperature of the outer surface of solar tubes does not decrease too much. It is because most of the solar radiation concentrates at the center of the solar tube at the positive X direction and the backside of the solar tube is not irradiated. Moreover, the coating on the solar tube surface is selected based on the recent study [32]. The emissivity of this coating in the infrared spectrum is only 0.4, which limits the thermal radiative loss of solar receivers. When the other coating with higher emissivity is applied, the thermal efficiency improvement by the composite tube design can be enhanced. Pyromark 2500 [33] is widely adopted in the solar thermal application for which the emissivity is around 0.88. When Pyromark 2500 is applied and all other simulation settings remain unchanged, the thermal efficiency improvements are 0.7% and 1.3% for the composite solar tubes with 3 mm and 4 mm wall thicknesses, respectively. Therefore, the composite tube design could not only decrease the thermal stress level of the solar tubes but also slightly increase the efficiency of solar-to-thermal energy conversion.

4.3. Influence of solar radiation intensity

In order to obtain an elevated outlet temperature of the heat transfer fluid, a large concentration ratio of solar radiation is needed. Therefore, the peak value of the solar radiation is enlarged from 700 kW/m 2 to 800 kW/m 2 to investigate the effectiveness of the composite tube design. The maximum temperature, maximum

thermal stress, and maximum total stress are summarized in Table 5.

Both the temperature and stress of all the solar tubes increase as the peak flux of solar radiation increases. The 316 stainless steel/ GRCop-84 composite solar tube still outperforms and decreases the maximum temperature and maximum thermal stress by 78.3 K and 31.6 MPa respectively when the tube wall thickness is 3 mm. Meanwhile, these values reach 118.3 K and 84.8 MPa as the wall thickness becomes 4 mm. However, compared to the cases with a lower peak solar flux, the relative decrease for thermal stress does not change significantly. For example, as for the stainless steel/ GRCop-84 composite solar tube with the 3 mm tube wall thickness, the relative decrease in thermal efficiency is 22.4% for the higher solar flux while this value is 19.8% for the relatively lower solar flux. On the other hand, the solar-to-thermal energy conversion efficiency increases as the overall temperature of solar tubes increases. It is because the thermal conductivity of sCO₂ increases in the temperature range of 700–1100 K at 20 MPa, which reduces the thermal resistance between the solar tube and the heat transfer fluid. However, the improvement of thermal efficiency due to the composite tube design is limited which is almost the same as that in the cases with the lower solar heat flux.

4.4. Long-term operation analyses

Based on the 30-year design requirement proposed by the Gen3 roadmap [1], the long-term operation performances such as fatigue and creep of solar tubes worth investigation. Fatigue of solar tubes represents the cycle weakening of the material caused by repeated stress, which is due to diurnal and complex weather conditions. Analytically, solar tubes should survive at least 10000 cycles in approximately 30 years. For a certain type of materials, the SN

Table 5 Performance of the solar tubes with $q_{\text{solar, peak}} = 800 \text{ kW/m}^2$.

Tube	Dimension	T _{max} (K)	η _t (%)	$\sigma_{t,max}$ (MPa)	$\sigma_{ m total,max}$ (MPa)
Α	$d_{\text{in}} = 6 \text{ mm t} = 3 \text{ mm}$	1014.6	77.1	126.1	162.4
В		968.9	77.4	115.2	155.7
C		998.4	77.1	130.8	172.6
D		920.1	77.5	99.2	133.9
E	$d_{in} = 7 \text{ mm t} = 4 \text{ mm}$	1095.6	75.4	178.1	218.8
F		1017.5	76.1	152.9	193.1
G		1074.9	75.6	192.0	232.4
Н		956.6	76.4	107.6	139.6

curve establishes the relationship between the stress amplitude and the total number of cycles to failure at a certain temperature. Meanwhile, the long-term exposure to stress under high temperature may cause creep issues to the material. Even though the stress level is below the yield strength of the material, the permanent deformation still occurs, leading to the failure of the material. The relationship of the rupture stress and the time of the material at a certain temperature can be depicted by equations such as the Larson-Miller relation and the Orr-Sherby-Dorn relation. For solar tubes, a minimum 100000 h operation time is needed. Moreover, in order to consider the coupling effect of fatigue and creep, the theory of cumulative damage is applied [3]. The weak positions of solar tubes are normally located at regions with highest temperature or largest stress.

For the composite solar tubes in this work, the protective and thermally conductive materials have different thermo-mechanical properties and should be analyzed respectively. Take Tube A and Tube B as examples. Considering that the fatigue strength of Inconel 718 is high, only the creep behavior is analyzed. The maximum allowable stresses for a 10000h rupture lifetime of Inconel 718 [34] and nickel [35] as a function of temperature are summarized in Table 6 and Table 7. It is found that the allowable stress increases dramatically as the temperature decreases, and nickel does not perform as good as Inconel 718 in the investigated temperature range.

In Tube A and Tube B, there are 1055630 nodes in each solar tube and the node coordinates, temperature and stress are extracted for creep behavior analysis. Two positions with maximum temperature or maximum stress in the area with Inconel 718 in Tube A and Tube B are presented in Table 8. The survived ratio is defined by the number of nodes surviving 100000h with respect to the total number of nodes. Although Inconel 718 is a high-temperature alloy with excellent mechanical strength, not all parts of pure Inconel 718 tube could be on service for 30 years under current simulation condition. By inserting a thermally conductive nickel layer, both the overall temperature and stress in the Inconel 718 layer decrease. The creep issue of Inconel 718 in the composite solar tube no longer exists.

On the other hand, the creep behavior of nickel in the composite solar Tube B is investigated and summarized in Table 9. It is found that 6.3% of the nickel material in the entire tube will potentially rupture during the 30 years operation. Therefore, the long-term thermo-mechanical properties at high temperature should be considered in the selection of the thermally conductive material. It should also be noted that the numerical model assumes a direct bonding between Inconel 718 and nickel, which overestimates the stress due to the mismatch of coefficients of thermal expansion at the interface of these two materials.

5. Perspective of design

5.1. Composite tube fabrication methods

Solar receiver tubes for Gen3 CSP systems should endure elevated temperature, high pressure, and severe stress under the long-term operation. Special attention should be paid for the material selection and fabrication methods of the composite solar tube to meet such requirements. Traditional manufacturing offers

Table 6Allowable stress for 10000h rupture lifetime of Inconel 718.

	•				
Temperature (°C)	704	649	593	538	482
Allowable stress (MPa)	42.8	236.9	500.1	745.9	962.2

Table 7Allowable stress for 10000h rupture lifetime of nickel

Temperature (°C)	650	595	540
Allowable stress (MPa)	19.1	37.8	49.5

Table 8Creep behavior of Inconel 718 in Tube A and Tube B.

Tube	Maximum temperature location		Maximum stress location		Survived ratio (%)
	T (K)	$\sigma_{ m total}$ (MPa)	T (K)	$\sigma_{ m total}$ (MPa)	
Α	985.4	88.7	808.3	146.7	99.7
В	944.7	62.4	802.8	142.8	100

Table 9 Creep behavior of nickel in Tube B.

Tube		Maximum temperature location		ım stress	Survived ratio (%)
	T(K)	$\sigma_{ m total}$ (MPa)	T(K)	$\sigma_{ m total}$ (MPa)	
В	913.5	32.7	809.9	56.0	94.7

various methods to fabricate composite tubes consisting of multiple metal materials. Generally, these methods could be divided into two types in terms of the bonding interface between materials, which are mechanical bonding processes and metallurgical bonding processes. The mechanical bonding processes such as cold rolling [36] and expanded joints [37] use mechanical force to combine different materials. The bonding of materials is not tight and delamination may occur at high temperature or under large axial force. The metallurgical bonding processes could achieve element diffusion between materials which provides more reliable interfaces. Typical methods involve hot rolling, co-extrusion, centrifugal casting etc. However, each method has its limitation during fabrication. For example, the centrifugal casting usually requires the weight of metal in the internal layer is lighter than that of the material at the external layer. The melting points of these materials should be different. Therefore, considering the high-temperature working environment of solar tubes, only the metallurgical bonding processes are more promising.

On the other hand, advanced manufacturing methods such as 3D printing present a flexible and precise way to fabricate composite structures with different materials. Bimetallic structures of Inconel 718 and GRCop-84 have been processed using laser engineered net shaping (LENS) [38]. Thermal diffusivity of the bimetallic structures was measured to be 11.33 mm²/s, which is a 250% increase as compared to pure Inconel 718. A 200 µm thick compositional layer was detected at the interface of Inconel 718 and GRCop-84 by energy dispersive spectroscopy (EDS). Liu et al. [39] achieved metallurgical diffusion for 316L stainless steel and C18400 copper alloy through selective laser melting (SLM). Tensile properties and microhardness of the bimetallic structure were characterized. Through optical microscopy and focused ion beam (FIB) imaging, a 700 μm compositional layer was found. Sing et al. [40] combined AlSi10Mg and C18400 copper alloy by SLM. The tensile property and microhardness of the composite structure were measured. Diffusion of elements was found by FIB imaging and the compositional layer thickness was estimated to be 200 μm . Therefore, 3D printing is a potential solution to the fabrication of composite solar tubes. The natural generated compositional layer is beneficial in reducing extra stress due to the mismatch for properties of different materials. Moreover, the study by Ho et al. [41]

adopted additively manufactured nickel-based superalloys for designing fractal-like solar receivers which proves the capability of 3D printing in fabricating complex geometry in high-temperature applications.

5.2. Future studies

Firstly, compared with the Inconel/nickel design, the application of copper alloy present far better improvement in reducing the stress level due to its large thermal conductivity. Considering the elevated working temperature, nickel-based superalloy is a potential candidate for replacing stainless steel. Therefore, the combination of nickel-based superalloy and copper alloy should be studied but the key challenge is the mismatch in coefficients of thermal expansion of these two materials. Secondly, the thermophysical and thermomechanical properties such as thermal conductivity and modulus of elasticity of composite structures should be characterized by experimental tests. In the current numerical models, materials in interfaces are directly bonded which allows idealized heat transfer and rigid transition in stress. The influence of the compositional layer on the material properties as well as temperature and stress distributions should be investigated. Thirdly, the composite solar tubes should be experimentally proved to be stable for the long-term operation at elevated temperature and high pressure. The metallurgical bonding between the thermally conductive layer and the protective layer should be sufficiently strong to prevent delamination. Particularly, the thermally conductive materials usually have poor performance regarding high-temperature creep property. Suitable heat treatment processes should be employed in order to improve creep and fatigue behaviors of the composite solar tubes.

6. Conclusions

The main conclusions are as follows:

- The thermally conductive layer reduces temperature gradient and maximum stresses, and the improvement becomes evident as the thermal conductivity goes higher. The maximum temperature decreases by 40.7 K and 69.0 K respectively for the Inconel 718/nickel and 316 stainless steel/GRCop-84 designs. The associated maximum thermal stress decreases by 4.1 MPa and 24.0 MPa, respectively.
- The reduction in temperature and thermal stress become obvious as the wall thickness of the solar tube and the intensity of solar radiation increase. For the 316 stainless steel/ GRCop-84 design, the maximum thermal stress could decrease relatively by 44.0% when the wall thickness and the peak solar heat flux are 4 mm and 800 kW/m², respectively.
- The thermal efficiencies of the solar tubes with 3 mm and 4 mm thickness increase by 0.4% and 0.7% respectively due to the lower surface temperature. The thermal efficiency could be improved by up to 1.3% when the emissivity of the coating increases from 0.4 to 0.88 for the solar tube with 4 mm thickness.
- The creep issue of high-temperature alloys could be alleviated due to the reduction in both temperature and stress levels. However, the creep issue in the thermally conductive layer should be solved as its creep behavior is usually poor.

CRediT authorship contribution statement

Shen Du: Investigation, Methodology, Formal analysis, Validation, Writing — original draft. **Zexiao Wang:** Investigation,

Validation, Writing — review & editing. **Sheng Shen:** Supervision, Project administration, Conceptualization, Validation, Writing — review & editing, Funding acquisition.

Declaration of competing interest

The authors declare that they have no known competing financial interests or personal relationships that could have appeared to influence the work reported in this paper.

Acknowledgements

This work was supported by the National Science Foundation under awards CMMI-1916110 and CBET-1931964.

Nomenclature

```
specific heat (J kg^{-1} \cdot K^{-1})
c_p
d_{\rm in}
             inner diameter of solar tube (m)
Е
             Young's modulus (Pa)
             turbulent kinetic energy (m^2 \cdot s^{-2})
k
L
            length of solar tube (m)
             pressure (Pa)
p
             solar heat flux (W m<sup>-2</sup>)
q
             radius of tube (m)
r
Т
             temperature (K)
             wall thickness of solar tube (m)
t
             velocity (m s<sup>-1</sup>)
и
х
             coordinate (m)
```

Greek symbols

```
\begin{array}{lll} \alpha & \text{coefficient of thermal expansion } (K^{-1}) \\ \varepsilon & \text{turbulent dissipation rate } (m^2 \cdot s^{-3}) \\ \eta & \text{thermal efficiency } (\%) \\ \lambda & \text{thermal conductivity } (W m^{-1} \cdot K^{-1}) \\ \mu & \text{dynamic viscosity } (Pa \cdot s) \\ \nu & \text{Poisson's ratio} \\ \rho & \text{density } (kg m^{-3}) \\ \sigma & \text{stress } (Pa) \end{array}
```

Subscripts

а	axial direction
f	fluid
i	inner surface of tube
max	maximum value
0	outer surface of tube
r	radial direction
S	solid
t	thermal
θ	tangential direction

References

- M. Mehos, C. Turchi, J. Vidal, M. Wagner, Z. Ma, C. Ho, W. Kolb, C. Andraka, A. Kruizenga, Concentrating Solar Power Gen3 Demonstration Roadmap, National Renewable Energy Lab, 2017.
- [2] Y.-L. He, Y. Qiu, K. Wang, F. Yuan, W.-Q. Wang, M.-J. Li, J.-Q. Guo, Perspective of concentrating solar power, Energy 198 (2020), 117373, https://doi.org/ 10.1016/j.energy.2020.117373.
- [3] T. Conroy, M.N. Collins, R. Grimes, A review of steady-state thermal and mechanical modelling on tubular solar receivers, Renew. Sustain. Energy Rev. 119 (2020), 109591, https://doi.org/10.1016/j.rser.2019.109591.
- [4] T.W. Neises, M.J. Wagner, A.K. Gray, Structural Design Considerations for Tubular Power Tower Receivers Operating at 650 C, American Society of Mechanical Engineers, 2014.
- [5] K. Nithyanandam, R. Pitchumani, Thermal and structural investigation of tubular supercritical carbon dioxide power tower receivers, Sol. Energy 135 (2016) 374–385, https://doi.org/10.1016/j.solener.2016.05.039.

- [6] J. Ortega, S. Khivsara, J. Christian, C. Ho, P. Dutta, Coupled modeling of a directly heated tubular solar receiver for supercritical carbon dioxide Brayton cycle: structural and creep-fatigue evaluation, Appl. Therm. Eng. 109 (2016) 979–987, https://doi.org/10.1016/j.applthermaleng.2016.06.031.
- [7] A. Montoya, M.R. Rodríguez-Sánchez, J. López-Puente, D. Santana, Numerical model of solar external receiver tubes: influence of mechanical boundary conditions and temperature variation in thermoelastic stresses, Sol. Energy 174 (2018) 912–922, https://doi.org/10.1016/j.solener.2018.09.068.
- [8] W.R. Logie, J.D. Pye, J. Coventry, Thermoelastic stress in concentrating solar receiver tubes: a retrospect on stress analysis methodology, and comparison of salt and sodium, Sol. Energy 160 (2018) 368–379, https://doi.org/10.1016/ i.solener.2017.12.003.
- [9] K. Wang, P.-S. Jia, Y. Zhang, Z.-D. Zhang, T. Wang, C.-H. Min, Thermal-fluid-mechanical analysis of tubular solar receiver panels using supercritical CO2 as heat transfer fluid under non-uniform solar flux distribution, Sol. Energy 223 (2021) 72–86, https://doi.org/10.1016/j.solener.2021.05.030.
- [10] K. Wang, Z.-D. Zhang, X.-Y. Zhang, C.-H. Min, Buoyancy effects on convective heat transfer of supercritical CO2 and thermal stress in parabolic trough receivers under non-uniform solar flux distribution, Int. J. Heat Mass Tran. 175 (2021), 121130, https://doi.org/10.1016/j.ijheatmasstransfer.2021.121130.
- [11] K. Wang, Z.-D. Zhang, M.-J. Li, C.-H. Min, A coupled optical-thermal-fluid-mechanical analysis of parabolic trough solar receivers using supercritical CO2 as heat transfer fluid, Appl. Therm. Eng. 183 (2021), 116154, https://doi.org/10.1016/j.applthermaleng.2020.116154.
- [12] Y. Chen, Y. Zhang, D. Wang, S. Hu, X. Huang, Effects of design parameters on fatigue—creep damage of tubular supercritical carbon dioxide power tower receivers, Renew. Energy 176 (2021) 520–532, https://doi.org/10.1016/ irenene.2021.05.069
- [13] Y. Chen, D. Wang, C. Zou, W. Gao, Y. Zhang, Thermal performance and thermal stress analysis of a supercritical CO2 solar conical receiver under different flow directions, Energy 246 (2022), 123344, https://doi.org/10.1016/ j.energy.2022.123344.
- [14] F. Wang, Y. Shuai, Y. Yuan, G. Yang, H. Tan, Thermal stress analysis of eccentric tube receiver using concentrated solar radiation, Sol. Energy 84 (10) (2010) 1809—1815, https://doi.org/10.1016/j.solener.2010.07.005.
- [15] F. Wang, Y. Shuai, Y. Yuan, B. Liu, Effects of material selection on the thermal stresses of tube receiver under concentrated solar irradiation, Mater. Des. 33 (2012) 284–291, https://doi.org/10.1016/j.matdes.2011.07.048.
- [16] V. Flores, R. Almanza, Behavior of the compound wall copper–steel receiver with stratified two-phase flow regimen in transient states when solar irradiance is arriving on one side of receiver, Sol. Energy 76 (1) (2004) 195–198, https://doi.org/10.1016/j.solener.2003.08.015.
- [17] S. Khanna, V. Sharma, S. Newar, T.K. Mallick, P.K. Panigrahi, Thermal stress in bimetallic receiver of solar parabolic trough concentrator induced due to non uniform temperature and solar flux distribution, Sol. Energy 176 (2018) 301–311, https://doi.org/10.1016/j.solener.2018.09.081.
- [18] A. Montoya, M.R. Rodríguez-Sánchez, J. López-Puente, D. Santana, Influence of longitudinal clips in thermal stresses and deflection in solar tubular receivers, Sol. Energy 198 (2020) 224–238, https://doi.org/10.1016/ j.solener.2020.01.030.
- [19] C. Frantz, A. Fritsch, R. Uhlig, ASTRID© advanced Solar Tubular Receiver Design: a powerful tool for receiver design and optimization, in: AIP Conference Proceedings, American Institute of Physics, 2017, 30017.
- [20] A. Fluent, 14.5 Theory Guide, ANSYS Inc, Canonsburg, PA, USA, 2012.
- [21] G.E. Rochau, Supercritical CO2 Brayton cycle development, in: Advance SMR Energy Conversion, Nuclear Energy, U.S. Department of Energy, 2014.
- [22] https://www.specialmetals.com/assets/smc/documents/inconel_alloy_718.

- pdf. Accessed 26 February 2020.
- [23] R. Powell, R. Tye, M. Hickman, The thermal conductivity of nickel, Int. J. Heat Mass Tran. 8 (5) (1965) 679–688, https://doi.org/10.1016/0017-9310(65) 00017-7
- [24] C.S. Kim, Thermophysical Properties of Stainless Steels, Argonne National Lab., (USA), 1975. Ill.
- [25] D.L. Ellis, D.J. Keller, M. Nathal, Thermophysical Properties of GRCop-84, National Aeronautics and Space Administration, 2000.
- [26] R. Farraro, R.B. McIellan, Temperature dependence of the Young's modulus and shear modulus of pure nickel, platinum, and molybdenum, Metall. Trans. A 8 (10) (1977) 1563–1565, https://doi.org/10.1007/BF02644859.
- [27] P. Hidnert, Thermal expansion of some nickel alloys, J. Res. Natl. Bur. Stand. 58 (2) (1957) 89–92, https://doi.org/10.6028/jres.058.011.
- [28] M. Grujicic, H. Zhao, Optimization of 316 stainless steel/alumina functionally graded material for reduction of damage induced by thermal residual stresses, Mater. Sci. Eng., A 252 (1) (1998) 117–132, https://doi.org/10.1016/S0921-5093(98)00618-2.
- [29] P. Desai, C. Ho, Thermal Linear Expansion of Nine Selected AISI Stainless Steels, Thermophysical and Electronic Properties Information Analysis Center, 1978.
- [30] D.L. Ellis, H.R. Gray, M. Nathel, Aerospace Structural Materials Handbook Supplement GRCop-84, 2001.
- [31] C. Dang, E. Hihara, In-tube cooling heat transfer of supercritical carbon dioxide. Part 1. Experimental measurement, Int. J. Refrig. 27 (7) (2004) 736–747, https://doi.org/10.1016/j.ijrefrig.2004.04.018.
- [32] H. Wang, I. Haechler, S. Kaur, J. Freedman, R. Prasher, Spectrally selective solar absorber stable up to 900 °C for 120 h under ambient conditions, Sol. Energy 174 (2018) 305–311, https://doi.org/10.1016/j.solener.2018.09.009.
 [33] C.K. Ho, A.R. Mahoney, A. Ambrosini, M. Bencomo, A. Hall, T.N. Lambert,
- [33] C.K. Ho, A.R. Mahoney, A. Ambrosini, M. Bencomo, A. Hall, T.N. Lambert, Characterization of Pyromark 2500 paint for high-temperature solar receivers, J. Sol. Energy Eng. 136 (1) (2013), https://doi.org/10.1115/1.4024031.
- [34] C. Brinkman, M. Booker, J. Ding, Creep and Creep-Rupture Behavior of Alloy 718, Oak Ridge National Lab., TN (USA), 1991.
- [35] https://www.specialmetals.com/assets/smc/documents/alloys/nickelduranickel/nickel-200-201.pdf. Accessed 6 March 2020.
- [36] G.P. Chaudhari, V. Acoff, Cold roll bonding of multi-layered bi-metal laminate composites, Compos. Sci. Technol. 69 (10) (2009) 1667–1675, https://doi.org/ 10.1016/i.compscitech.2009.03.018.
- [37] W. Xu, Z. Zhang, K. Huang, D. Shan, Effect of heat treatment and initial thickness ratio on spin bonding of 3A21/5A03 composite tube, J. Mater. Process. Technol. 247 (2017) 143–157, https://doi.org/10.1016/ j.jmatprotec.2017.04.014.
- [38] B. Onuike, B. Heer, A. Bandyopadhyay, Additive manufacturing of Inconel 718—copper alloy bimetallic structure using laser engineered net shaping (LENSTM), Addit. Manuf. 21 (2018) 133—140, https://doi.org/10.1016/ i.addma.2018.02.007.
- [39] Z.H. Liu, D.Q. Zhang, S.L. Sing, C.K. Chua, L.E. Loh, Interfacial characterization of SLM parts in multi-material processing: metallurgical diffusion between 316L stainless steel and C18400 copper alloy, Mater. Char. 94 (2014) 116–125, https://doi.org/10.1016/j.matchar.2014.05.001.
- [40] S.L. Sing, L.P. Lam, D.Q. Zhang, Z.H. Liu, C.K. Chua, Interfacial characterization of SLM parts in multi-material processing: intermetallic phase formation between AlSi10Mg and C18400 copper alloy, Mater. Char. 107 (2015) 220–227, https://doi.org/10.1016/j.matchar.2015.07.007.
- [41] C.K. Ho, J.M. Christian, J. Yellowhair, J. Ortega, C. Andraka, Fractal-like receiver geometries and features for increased light trapping and thermal efficiency, in: AIP Conference Proceedings, American Institute of Physics, 2016, 30021.